

The Sloan Digital Sky Survey Reverberation Mapping Project: Mg II Lag Results from Four Years of Monitoring

Y. Homayouni , Jonathan R. Trump , C. J. Grier , Keith Horne , Yue Shen , W. N. Brandt , W. N. B D. P. Schneider^{6,7}, D. A. Starkey³, Dmitry Bizyaev^{14,18}, Kaike Pan¹⁴, Daniel Oravetz¹⁴, and Audrey Simmons¹⁴ University of Connecticut, Department of Physics, 2152 Hillside Road, Unit 3046, Storrs, CT 06269-3046, USA; yasaman.homayouni@uconn.edu ² Steward Observatory, The University of Arizona, 933 North Cherry Avenue, Tucson, AZ 85721, USA ³ SUPA Physics and Astronomy, University of St. Andrews, Fife, KY16 9SS, Scotland, UK ⁴ Department of Astronomy, University of Illinois at Urbana-Champaign, Urbana, IL 61801, USA ⁵ National Center for Supercomputing Applications, University of Illinois at Urbana-Champaign, Urbana, IL 61801, USA ⁶ Dept. of Astronomy and Astrophysics, The Pennsylvania State University, 525 Davey Laboratory, University Park, PA 16802, USA Institute for Gravitation and the Cosmos, The Pennsylvania State University, University Park, PA 16802, USA Department of Physics, 104 Davey Lab, The Pennsylvania State University, University Park, PA 16802, USA Department of Physics and Astronomy, University of Utah, Salt Lake City, UT 84112, USA Harvard-Smithsonian Center for Astrophysics, 60 Garden Street, Cambridge, MA 02138, USA Department of Physics and Astronomy, York University, Toronto, ON M3J 1P3, Canada ¹² Kavli Institute for Astronomy and Astrophysics, Peking University, Beijing 100871, People's Republic of China 13 Department of Astronomy, School of Physics, Peking University, Beijing 100871, People's Republic of China ¹⁴ Apache Point Observatory and New Mexico State University, P.O. Box 59, Sunspot, NM 88349-0059, USA ¹⁵ Department of Astronomy, The Ohio State University, 140 West 18th Avenue, Columbus, OH 43210, USA ¹⁶ Center for Cosmology and AstroParticle Physics, The Ohio State University, 191 West Woodruff Avenue, Columbus, OH 43210, USA Space Telescope Science Institute, 3700 San Martin Drive, Baltimore, MD 21218, USA Sternberg Astronomical Institute, Moscow State University, Moscow, Russia Received 2020 May 7; revised 2020 July 27; accepted 2020 July 28; published 2020 September 21

Abstract

We present reverberation mapping results for the Mg II $\lambda 2800$ Å broad emission line in a sample of 193 quasars at 0.35 < z < 1.7 with photometric and spectroscopic monitoring observations from the Sloan Digital Sky Survey Reverberation Mapping project during 2014–2017. We find significant time lags between the Mg II and continuum lightcurves for 57 quasars, and define a "gold sample" of 24 quasars with the most reliable lag measurements. We estimate false-positive rates for each lag that range from 1% to 24%, with an average false-positive rate of 11% for the full sample and 8% for the gold sample. There are an additional \sim 40 quasars with marginal Mg II lag detections, which may yield reliable lags after additional years of monitoring. The Mg II lags follow a radius–luminosity relation with a best-fit slope that is consistent with $\alpha=0.5$, but with an intrinsic scatter of 0.36 dex that is significantly larger than found for the H β radius–luminosity relation. For targets with SDSS-RM lag measurements of other emission lines, we find that our Mg II lags are similar to the H β lags and \sim 2–3 times larger than the C IV lags. This work significantly increases the number of Mg II broad-line lags and provides additional reverberation-mapped black hole masses, filling the redshift gap at the peak of supermassive black hole growth between the H β and C IV emission lines in optical spectroscopy.

Unified Astronomy Thesaurus concepts: Active galaxies (17); Galaxy nuclei (609); Quasars (1319); Active galactic nuclei (16)

Supporting material: figure sets, machine-readable table

1. Introduction

Observations over more than two decades have shown that supermassive black holes (SMBHs) exist at the center of every massive galaxy and that several galaxy properties are correlated with the mass of the central SMBH (Magorrian et al. 1998; Gültekin et al. 2009; Kormendy & Ho 2013). Understanding the "co-evolution" of galaxies and their SMBHs, as implied by these correlations, depends critically on accurately measuring SMBH masses over cosmic time.

The masses of nearby SMBHs have been measured using high spatial resolution observations of stellar or gas dynamics (for a review, see Kormendy & Ho (2013)), or, in one specific case of M87, using the black hole "shadow" (Event Horizon Telescope Collaboration et al. 2019). However, these techniques are not yet possible for higher-redshift galaxies

 $(z\gtrsim0.3),$ even with next generation facilities. Beyond the local universe, reverberation mapping (RM; e.g., Blandford & McKee 1982; Peterson 1993, 2004) is the primary technique for measuring SMBH masses. Nearly all rapidly accreting SMBHs, observed as quasars or broad-line active galactic nuclei (AGNs), exhibit widespread variability on timescales of weeks to years (e.g., MacLeod et al. 2012). RM measures the time lag, τ , between the variability in the continuum and the broad emission lines. In the standard "lamp post" model (Cackett & Horne 2006), this time delay is simply the light travel distance between the central SMBH disk and the broad line-emitting region (BLR). Assuming that the BLR motion is gravitational,

$$M_{\rm BH} = \frac{fR_{\rm BLR} \,\Delta V^2}{G} \tag{1}$$

determines the virial product, where G is the gravitational constant, $R_{\rm BLR} = c\tau$ is the characteristic size of the BLR, ΔV is the broad emission line width, and f is a dimensionless factor of order unity that depends (in ways still not fully understood) on the orientation, structure, and geometry of the BLR.

Depending on quasar redshift, different emission lines are used to find the correlation between BLR and continuum lightcurves. The Balmer lines H β and H α are well-studied in numerous optical RM observations of broad-line AGN at z < 1 (Peterson et al. 1991; Kaspi et al. 2000; Peterson 2004; Bentz et al. 2009, 2010; Denney et al. 2010; Grier et al. 2012, 2017; Barth et al. 2015; Du et al. 2015, 2016a, 2016b; Hu et al. 2015; Shen et al. 2016b; Pei et al. 2017), with a total of \sim 100 mass measurements, mostly at z < 0.3.

There are an additional \sim 60 RM measurements of the C IV λ 1549 emission line for quasars at z>1.3 (Kaspi et al. 2007; Lira et al. 2018; Grier et al. 2019; Hoormann et al. 2019; Shen et al. 2019a). At intermediate redshifts (0.7 $\lesssim z \lesssim 1.5$), Mg II λ 2800 Å is the strongest broad line in the observed-frame optical. However, there have been only a handful of successful detections of Mg II lags in higher-redshift AGN (Shen et al. 2016b; Lira et al. 2018; Czerny et al. 2019), with many other attempts failing (Trevese et al. 2007; Woo 2008; Cackett et al. 2015), mostly because the Mg II line is generally less variable than the H β broad line (Sun et al. 2015). The limited number of Mg II RM measurements from observed-frame ultraviolet (UV) spectroscopy of nearby AGN show lags that are broadly consistent with the H β lags of the same objects (Clavel et al. 1991; Reichert et al. 1994; Metzroth et al. 2006).

RM masses over $1 \lesssim z \lesssim 2$ are particularly desirable because these epochs represent the peak of SMBH accretion (e.g., Section 3.2 of Brandt & Alexander (2015)): the current lack of Mg II RM measurements fundamentally limits our understanding of SMBH growth.

RM studies of local AGN have established a correlation between the H β broad-line radius and the (host-subtracted) AGN luminosity (Kaspi et al. 2000; Bentz et al. 2013). This enables scaling relations to estimate SMBH masses solely from broad-line width and luminosity (Vestergaard & Peterson 2006). There have been attempts to calibrate Mg II single-epoch masses derived from the RM-based H β radius-luminosity relation in quasars with both broad lines, building analogous single-epoch mass estimators from Mg II (McLure & Jarvis 2002; Vestergaard & Osmer 2009; Shen et al. 2011; Bahk et al. 2019). However, these Mg II mass estimators are plagued by bias (Shen & Kelly 2012), and some aspects of the Mg II variability behavior suggest that an intrinsic Mg II radiusluminosity relation may not exist (Guo et al. 2020a). Additional RM studies of Mg II are critically needed to understand if the Mg II line can be used for both single-epoch and RM masses, and in turn if it can be used to complete our understanding of SMBH mass buildup through intermediate redshifts.

In this work, we present Mg II lag results from four years of spectroscopic and photometric monitoring by the Sloan Digital Sky Survey Reverberation Mapping (SDSS-RM) project. Section 2 describes the details of the SDSS-RM campaign and sample selection criteria, and our methods of time series analysis and lag identification are presented in Section 3. In Section 4, we present tests of lag reliability that motivate our ultimate lag selection criteria and alias removal. Section 5 presents our final lag results, comparing the measured Mg II lags with the H β and C IV lags of the same quasars along with a

Mg II $R\!-\!L$ relation. Finally, we discuss and summarize our work in Section 6. Throughout this work, we adopt a $\Lambda {\rm CDM}$ cosmology with $\Omega_{\Lambda}=0.7,~\Omega_{M}=0.3,$ and $H_{0}=70~{\rm km~s}^{-1}~{\rm Mpc}^{-1}.$

2. Data

2.1. Sample Selection

Our sample is drawn from the 849 quasars monitored by SDSS-RM, with spectroscopy and photometry in a single 7 deg² field observed every year from January–July since 2014 (see Shen et al. 2015a, 2019b). The primary goal of SDSS-RM is to measure lags and black hole masses for >100 quasars spanning a wide range of redshift and AGN properties, using $H\beta$ (Shen et al. 2016b; Grier et al. 2017), C IV (Grier et al. 2019; Shen et al. 2019a), and Mg II (Shen et al. 2016b; this work). SDSS-RM has also been successful in several related studies of quasar variability (Sun et al. 2015; Dexter et al. 2019), quasar emission-line properties (Denney et al. 2016a, 2016b; Shen et al. 2016a; Wang et al. 2019), broad absorption line (BAL) variability (Grier et al. 2016; Hemler et al. 2019), the relationship between SMBH and host galaxy properties (Matsuoka et al. 2015; Shen et al. 2015b), and quasar accretion-disk lags (Homayouni et al. 2019). SDSS-RM is a purely magnitude-limited sample ($i_{psf} < 21.7$ mag), in contrast to previous RM studies that selected samples based on quasar variability, lag detectability, and large emission-line equivalent width. This means that SDSS-RM quasars span a broader range of redshift and other quasar properties compared to previous RM studies (Shen et al. 2015a).

To select the targets for this study, we first require that Mg II is in the observed-frame optical spectra (i.e., 0.35 < z < 2.6). After inspecting the SDSS-RM root mean square (rms) spectra, we found that for ~70% of the selected targets with z > 1.7, the Mg II line profile is weak with respect to the continuum emission and contaminated by (variable) sky lines, and thus we restrict our parent sample to the 453 quasars with 0.35 < z < 1.7.

To ensure that Mg II lightcurves are sufficiently variable and have the potential for lag detection, we require a minimum signal-to-noise ratio (S/N) of the Mg II variability, defined as SNR2 $\equiv \sqrt{\chi^2 - \text{DOF}}$. Here, χ^2 is the squared deviation of the fluxes relative to the median with respect to the estimated uncertainties, and DOF = $N_{\text{lightcurve}} - 1$ is the degrees of freedom of each lightcurve. SNR2 quantifies the deviation from the null hypothesis of no variability, where SNR2 \sim 1 indicates that the variability is dominated by the noise. This quantity is calculated by the PrepSpec (Alard & Lupton 1998) software that is used to flux-calibrate the lightcurves (see Section 2.2 for details). We follow Grier et al. (2019) and require our targets to be significantly variable, with SNR2 > 20. There are 198 quasars with both 0.35 < z < 1.7 and Mg II SNR2 > 20. This SNR2 threshold rejects a larger fraction of Mg II targets than it did for the H β and C IV samples used in Grier et al. (2017, 2019), as Mg II is generally less variable than the other strong broad lines in quasars (Sun et al. 2015).

Finally, we reject two targets that have Mg II BALs and three targets with weak Mg II emission that have average line fluxes consistent with zero. This results in a Mg II subsample of 193 quasars in which we search for lags. The properties of these targets are summarized in Figure 1, and the details of each target are listed in Table 1.

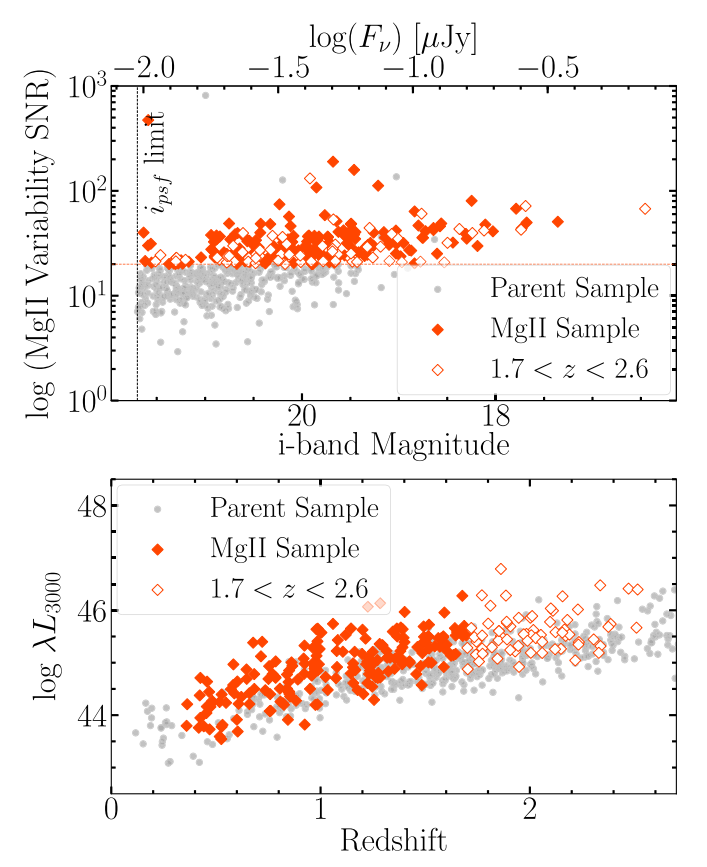


Figure 1. SDSS-RM parent sample of 849 quasars (gray points) and the Mg II subsample of 193 quasars (red filled points). Mg II subsample is selected to have significant Mg II variability (top panel; see Section 2.1 for more detail) and redshifts within 0.35 < z < 1.7, such that Mg II is in the observed spectral range and uncontaminated by variable sky emission. Open red symbols show z > 1.7 quasars where the Mg II emission line is variable but frequently affected by telluric contamination. In this paper, all of our analysis is performed on the subsample of 193 targets (filled symbols) with 0.35 < z < 1.7.

2.2. Spectroscopy

The SDSS-RM monitoring includes multi-epoch spectroscopy from the BOSS spectrograph (Dawson et al. 2013; Smee et al. 2013) mounted on the 2.5 m SDSS telescope (Gunn et al. 2006), covering wavelengths of 3650–10400 Å with a spectral resolution of $R \sim 2000$. We use four years of SDSS-RM spectroscopic observations, obtained annually during dark/ gray observing windows from 2014 January to 2017 July, for a total of 68 spectroscopic epochs. During the first year, SDSS-RM obtained a total of 32 epochs with a median cadence of 4 days for the spectroscopy and 2 days for the photometry discussed below, set by weather conditions and scheduling constraints. The following three years had a sparser cadence, with 12 epochs obtained over the 6 month observing window each year. Figure 2 shows the median S/N of the continuum and Mg II emission line in each epoch for all of the quasars in the Mg II subsample. This S/N is computed from the median ratio of the intercalibrated fluxes and the uncertainties (see Section 2.4 for more detail) at each epoch.

The spectroscopic data are initially processed through the standard BOSS reduction pipeline (Dawson et al. 2016; Blanton et al. 2017), including flat-fielding, spectral extraction, wavelength calibration, sky subtraction, and flux calibration. The SDSS-RM data are then processed by a secondary custom flux-calibration pipeline that uses position-dependent calibration vectors to improve the spectrophotometric calibrations; see Shen et al. (2015a) for

details. Finally, PrepSpec is used to further improve the relative spectrophotometry and remove any epoch-dependent calibration errors by optimizing model fits to wavelength-dependent and time-dependent continuum and broad-line variability patterns using the fluxes of the narrow emission lines; see Shen et al. (2016b) for details. PrepSpec also computes a maximum-likelihood S/N for the Mg II variability (along with similar variability S/N estimates for the continuum and other emission lines) that is used in our sample selection process (see Section 2.1).

We use the calibrated PrepSpec spectra to compute synthetic photometry in the g and i bands by convolving the calibrated spectra with the SDSS filter response function (Fukugita et al. 1996; Doi et al. 2010). The synthetic flux error is computed using the quadratic sum of errors in the measured spectra, errors in the shape of the response function, and the errors in PrepSpec calibration.

To improve the overall quality of the continuum and line lightcurves, a small number of epochs (1%) are rejected as outliers if offset from the median flux by more than five times the error-normalized median absolute deviation (NMAD). This outlier rejection effectively removes the rare cases of incorrect fiber placement on the SDSS-RM plates.

2.3. Photometry

SDSS-RM is supported by ground-based photometry from the 3.6 m Canada–France–Hawaii Telescope (CFHT) Mega-Cam (Aune et al. 2003) and the 2.3 m Steward Observatory Bok telescope 90" (Williams et al. 2004) imagers. Photometry was obtained in the g and i filters over the full SDSS-RM field, with the same January–July time coverage over 2014–2017 and a faster cadence than the spectroscopy. The top panels of Figure 2 show the average S/N of the g and i flux densities at each photometric epoch for the 193 quasars.

The photometric lightcurves are extracted from the images using image subtraction as implemented in the ISIS software package (Alard 2000). ISIS aligns all the images and picks a set of images with the best seeing to build a reference image. A scaled reference image, convolved by the point-spread function (PSF) at that epoch, is then subtracted from each image to leave only the variable flux. Lightcurves are extracted from the subtracted images and the flux of the quasar in the reference image is added to produce the final lightcurve.

The image subtraction is performed for each individual telescope, filter, CCD, and field to produce the g and i lightcurves (Kinemuchi et al. 2020).

We apply the same outlier rejection method that was implemented on the Mg II lightcurves, removing data points that are more than five times the NMAD from the median lightcurve flux. This step excludes data with incorrect photometry due to clouds, nearby bright stars, or detector edges.

2.4. Lightcurve Merging

Photometric monitoring using three different observing sites ensures that SDSS-RM has sufficient cadence to produce well-sampled continuum lightcurves. However, combining the multisite observations requires careful treatment of the differences in seeing, calibration, filter response, telescope throughput, and other site-dependent properties. We use the Continuum REprocessing AGN Markov Chain Monte Carlo (CREAM; Starkey et al. 2016) model to intercalibrate the lightcurves obtained at different sites, following Grier et al. (2017, 2019).

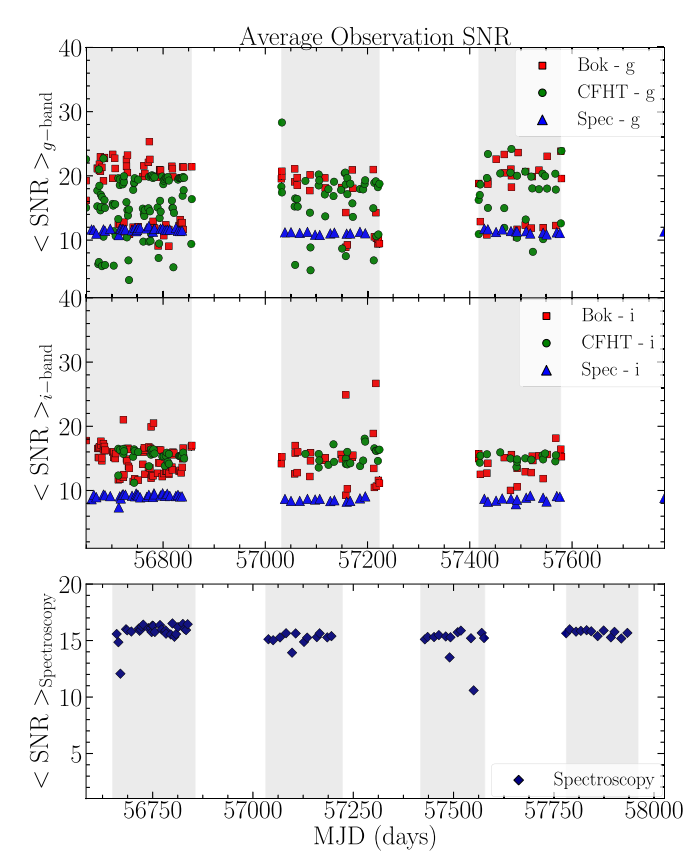


Figure 2. Average S/N and time coverage of the SDSS-RM g (top panel), i (middle panel), and Mg II (bottom panel) monitoring observations. SDSS-RM monitors 849 targets every year from 2014 January to June (shaded in gray), with a median spectroscopic cadence of 4 days during the first year. Each point represents the average S/N of the Mg II emission line for the 193 quasars in our Mg II sample observed at that epoch.

CREAM models the lightcurves using a power-law prior for the shape of the lightcurve power spectrum, which resembles the observed behavior of AGN lightcurves on short timescales (MacLeod et al. 2010; Starkey et al. 2016). To intercalibrate the lightcurves, the CREAM model is fit to the individual photometric lightcurves from each telescope, filter, and pointing, using a delta-function transfer function and zero lag. Each lightcurve is then rescaled and matched to the model using a multiplicative and additive factor, including rescaled flux uncertainties.

The g and i photometry are merged into a single continuum lightcurve, since the lag between these continuum bands is negligible compared to the expected Mg II emission line lags (e.g., Fausnaugh et al. 2016). We additionally use CREAM to rescale the Mg II lightcurve uncertainties, with extra variance as an additive component and a scale factor as a multiplicative component added in quadrature, while allowing the lag and transfer function to be free parameters. An example of the CREAM lightcurve merging is shown in Figure 3.

Occasionally, the photometric g and i lightcurves are affected by contamination from broad emission-line variability. We computed the broad-line variability contamination for the Mg II parent sample and identified four targets that have $>\!10\%$ contamination in the g band and five (different) targets that have $>\!10\%$ contamination in the i band. These broad-line contaminated lightcurves are excluded from the merged continuum lightcurves.

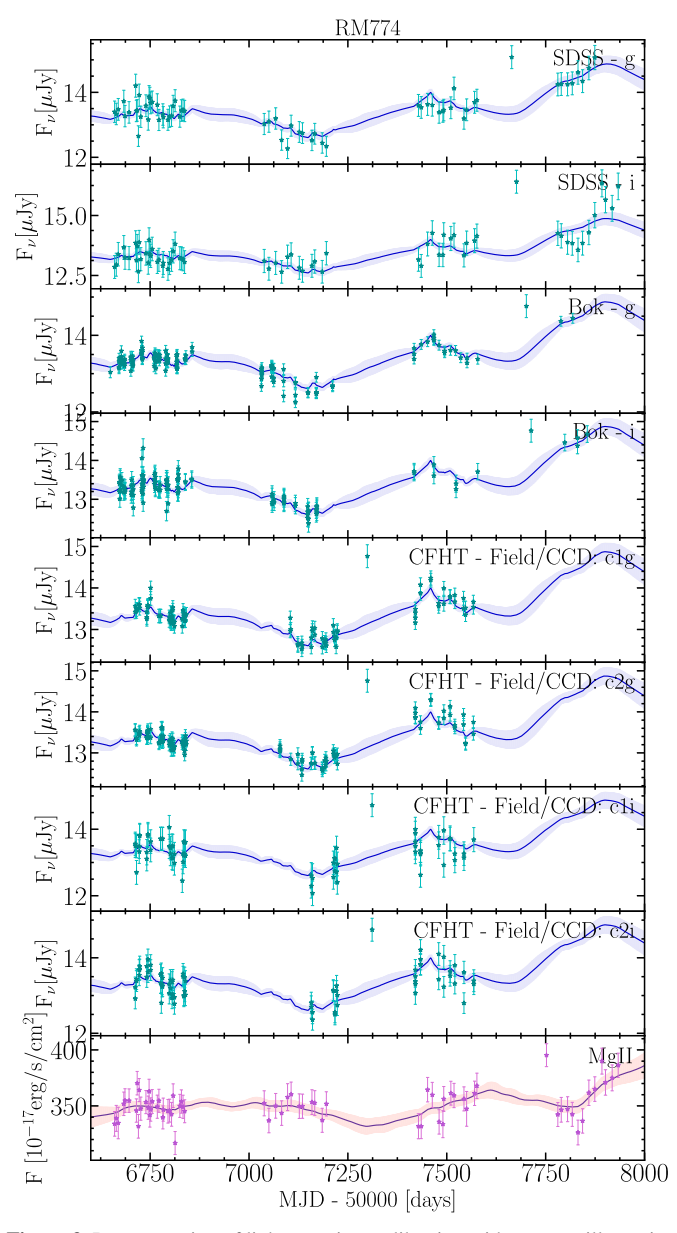


Figure 3. Demonstration of lightcurve intercalibration with CREAM, illustrating model fits and rescaled data for the 4 yr lightcurves of RMID 774. Each panel shows the individual pre-merged lightcurve from each observing site in both the g and i filters; CFHT observations have multiple lightcurves from different fields and CCDs in $\sim 25\%$ of the sample. CREAM model prediction and rescaled lightcurves are shown for the post-merged data (cyan for continuum lightcurves and pink for emission-line lightcurve).

We additionally reject photometric lightcurves from individual pointing/CCDs that are visual outliers compared to the other photometric lightcurves of the same object. These rejected outlier lightcurves are generally associated with imaging problems associated with detector edges, and they represent <1% of the observed lightcurves.

3. Time Series Analysis

We measure lags from the SDSS-RM lightcurves following the same approach as Grier et al. (2019), with two widely used time series analysis methods adapted for multiyear observations: JAVELIN (Zu et al. 2011) and CREAM (Starkey et al. 2016). We do not use the older Interpolated Cross Correlation

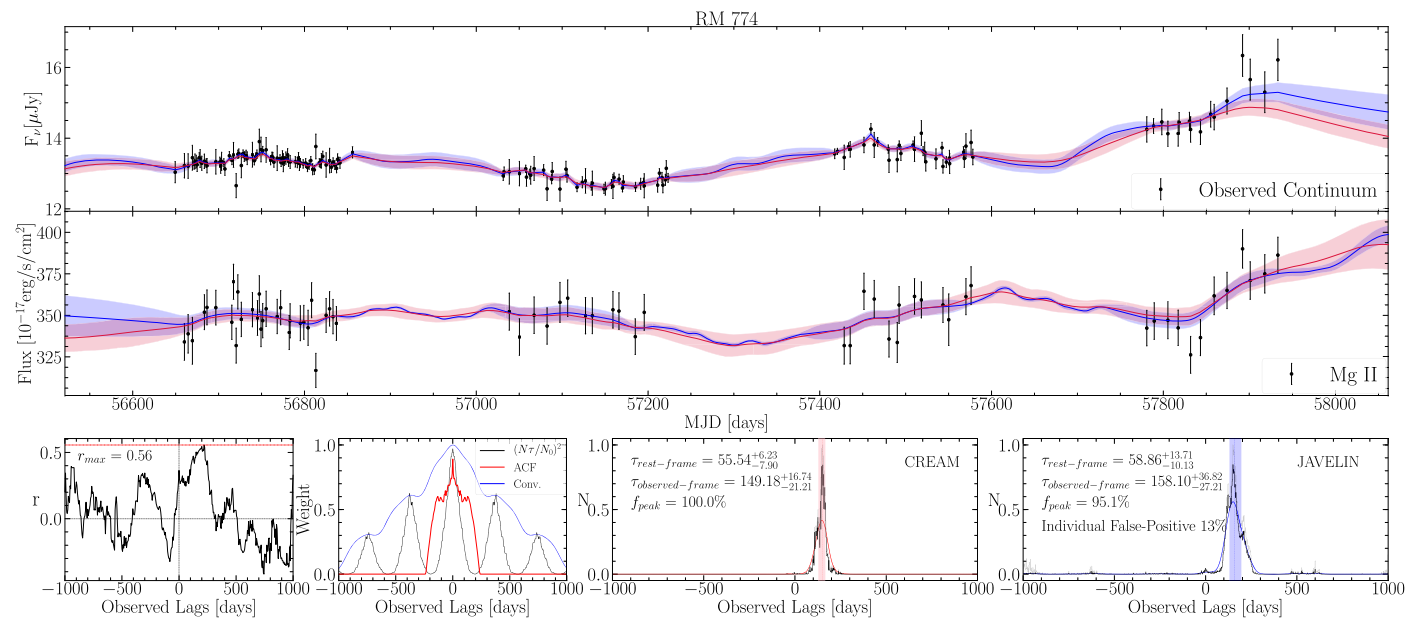


Figure 4. Continuum lightcurve (top panel) and Mg II lightcurve (middle panel) for RM ID 774 along with lag posteriors (bottom panels). In the top two panels, both JAVELIN (blue) and CREAM (red) model fits are shown for the continuum and Mg II line lightcurves. The displayed lightcurves are plotted with nightly averages for clarity, although the time-series analysis is computed from the nonaveraged observations. Bottom left: the cross-correlation coefficient computed between the continuum and Mg II line lightcurve with its maximum displayed by a horizontal red line. Second from the left: the applied weights for our alias removal, with the $[N(\tau)/N(0)]^2$ overlap between lightcurves in black, the continuum autocorrelation function in red, and the final applied weight in blue, obtained from the convolution of the black and red curves. Third and fourth from the left: the unweighted (gray) and weighted (black) lag PDFs computed by JAVELIN and CREAM. The colored curves indicate the smoothed lag PDFs, which are used to find the lag bins. The primary lag is indicated by the colored vertical line, with its 16th/84th percentile uncertainties enclosed by the colored shading. Available as a figure set for the full sample of 193 AGN.

(The complete figure set (193 images) is available.)

Function (i.e., ICCF) method (Gaskell & Sparke 1986; Gaskell & Peterson 1987; Peterson 2004) that was commonly used in previous RM studies. ICCF relies on linear interpolation and is less reliable than JAVELIN and CREAM when applied to SDSS-RM and similar RM programs with sparsely sampled monitoring (Grier et al. 2017; Li et al. 2019), and ICCF also generally overestimates lag uncertainties (Yu et al. 2020). For comparison with ICCF lag measurements, we calculate the Pearson coefficient r between the linearly interpolated continuum and emission line lightcurves (bottom left panel of Figure 4).

3.1. Javelin

JAVELIN (Zu et al. 2011) assumes that the quasar variability lightcurve can be modeled by a damped random walk (DRW) process. The DRW description of quasar stochastic variability is well-motivated by observations (Kelly et al. 2009; MacLeod et al. 2010, 2012; Kozłowski 2016) for the variability timescales probed by SDSS-RM. JAVELIN uses a Markov Chain Monte Carlo approach using a maximum likelihood method to fit a DRW model to the continuum and emission-line lightcurves, assuming that the line lightcurve is a shifted, scaled, and smoothed version of the continuum lightcurve.

We allow the DRW amplitude to be a free parameter, but we fix the DRW damping timescale to 300 days because this quantity is not well-constrained by the SDSS-RM monitoring duration. We also tested damping timescales of 100, 200, and 500 days; as expected (e.g., Yu et al. 2020), we found no significant differences in the measured lags. The response of the line lightcurve is parameterized as a top-hat transfer function, assuming a lag and scale factor that is a free parameter with a fixed transfer function width of 20 days. Our observations are not sufficient to constrain the transfer function widths, resulting in

unphysical transfer function widths if left as a free parameter in JAVELIN. A 20 day transfer function width is sufficiently short compared to the expected lag. We tested transfer function widths of 10 and 20 days, motivated by velocity resolved lag observations (Grier et al. 2013; Pancoast et al. 2018), with no significant differences in the measured lags. A broader transfer function width of 40 days resulted in significantly different lags for only $\sim\!\!10\%$ of our sample. We adopt a lag search range of ± 1000 days, chosen to be less than the $\sim\!\!1300$ day monitoring duration from 2014 January to 2017 July. JAVELIN returns a lag posterior distribution from 62500 MCMC simulations, which is used to compute the lag and its uncertainty.

3.2. Cream

CREAM (Starkey et al. 2016) models the driving lightcurve variability with a random walk power spectrum prior $P(f) \propto f^{-2}$, motivated by the lamp post model (Cackett et al. 2007). The observed continuum lightcurves are only a proxy for the ionizing continuum, and so CREAM constructs a new driving lightcurve and models both the observed continuum and line emission as smoothed versions of this ionizing continuum model. CREAM fits a top-hat response function to the emission-line lightcurve, returning a lag posterior probability distribution while simultaneously intercalibrating the lightcurves.

Here, we use a Python implementation of CREAM called PyceCREAM. We adopt a high-frequency variability limit of 0.3 cycles per day and normal priors of $\mathcal{N}(1.2, 0.2)$ for the multiplicative error rescaling parameter and normal priors of $\mathcal{N}(0.5, 0.1)$ for the variance expansion parameter. As with

¹⁹ https://github.com/dstarkey23/pycecream

JAVELIN, we allow CREAM to probe a lag search range of $\pm 1000 \mbox{ days}.$

4. Lag Reliability and Significance

4.1. Lag Identification and Alias Removal

The posterior lag distributions from JAVELIN or CREAM occasionally contain a primary peak accompanied by other, less significant peaks. The presence of multiple peaks in the posterior lag distribution, also known as aliasing, is a potential outcome of lag detection with sparse sampling data. Aliasing can be caused by matches of weak variability features between the continuum and line lightcurves, because the lag detection MCMC algorithm does not converge, and/or by quasi-periodic variations. The presence of seasonal gaps in multiyear RM data might also cause the lag detection algorithm to inappropriately prefer lags that fall in seasonal gaps where the lightcurve is interpolated with the DRW model prediction in JAVELIN or CREAM rather than directly constrained by observations.

To address the aliasing, we adopt the same lag identification and alias removal procedures as Grier et al. (2019), based on applying a weight to the posterior lag distribution. The weight prior avoids aliased solutions by penalizing parts of the lag posterior that have little overlap between the observed continuum and emission-line lightcurves. This ensures that the final lag search range and lag uncertainties correspond to observationally motivated lags.

There are two components to the weight prior. For the first component, we use the number of overlapping observed epochs between each target's continuum and line lightcurve, given a time lag τ . If this lightcurve shift results in fewer overlaps between the observed continuum and line lightcurves (e.g., time lags of ~ 180 days), it is less probable for the lag to be recovered, while having more overlapping data points leads to a more secure lag detection. Following Grier et al. (2019), we adopt the overlapping probability weight $P(\tau) = [N(\tau)/N(0)]^2$, where $N(\tau)$ corresponds to the number of overlapping continuum lightcurve and τ -shifted line lightcurve points and N(0) is the number of overlapping data points with no lag, i.e., $\tau=0$. We force the weight prior to be symmetric by computing $P(\tau)$ for the line lightcurve shifted by $\tau>0$ with respect to the continuum and then assigning the same values at $\tau=-\tau$.

The second component of the weight prior uses the autocorrelation function (ACF) as a measure of how the continuum variability behavior affects our ability to detect lags. For example, a narrow autocorrelation function indicates rapid variability, in which case seasonal gaps are likely to have consequential effects on our lag detection sensitivity. The final weight prior is the convolution between the overlapping probability, $P(\tau)$, and the continuum lightcurve ACF (forcing ACF = 0 when it drops below zero). We refer to the application of the final weight to the posterior lag distributions of JAVELIN and CREAM as the *weighted* lag posteriors.

To identify the time lag from the weighted posterior lag distribution, we first smooth the weighted posteriors by a Gaussian filter with a width of 12 days, which helps to identify the peaks in the weighted lag posteriors. The respective primary peaks in the weighted and smoothed lag posteriors are identified from the peak with the largest area in each, and smaller ancillary peaks in the lag posterior are considered insignificant for our lag identification. Within this primary

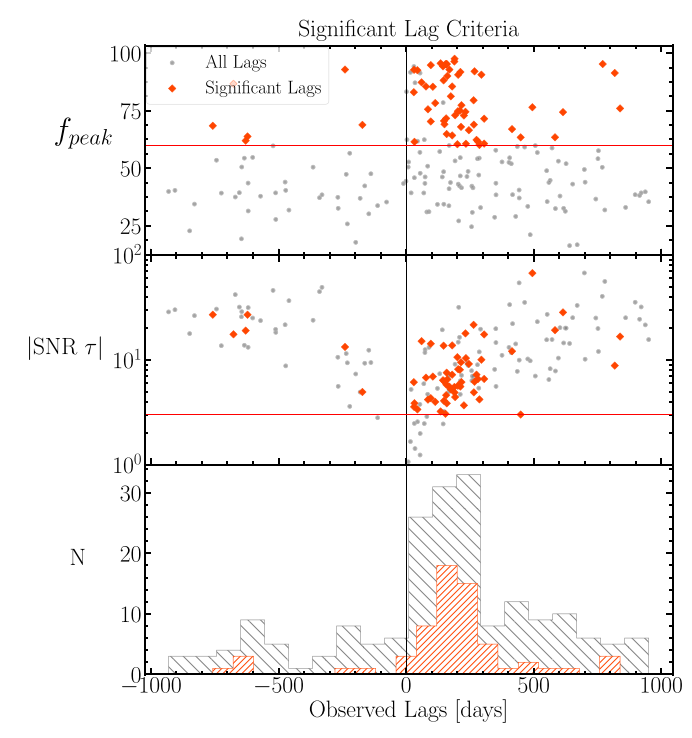


Figure 5. Lag significance criteria for the JAVELIN-measured lags. Top: fraction of the lag posterior within the primary peak, $f_{\rm peak}$. Middle: absolute value of the lag S/N. Bottom: histogram of measured lags for the full sample of 193 AGN (gray) and the sample of significant lags (red). Sample includes 57 significant and positive lags that meet both the $f_{\rm peak}$ and $|{\rm S/N}|$ criteria (red lines in the top 2 panels, defined in Section 4.2), with an average false-positive rate of 11%.

peak, the expected lag, τ , is determined from the median of the *unweighted* lag posteriors, and the lag uncertainty is calculated from the 16th and 84th percentiles. Figure 4 provides an example of our alias removal approach and lag detection.

4.2. "Significant" Lag Criteria

Our lag identification approach removes many secondary peaks and aliases. We require several additional criteria to ensure the final reported lags are statistically meaningful, following an approach similar to that of Grier et al. (2019). The first criterion is to require that 60% of the weighted lag posteriors samples are within the primary peak, i.e., $f_{\rm peak} > 60\%$. The primary peak, defined in the previous subsection, is the region of the smoothed lag posterior between local minima with the largest area. The $f_{\rm peak}$ requirement ensures a reliable lag solution and removes cases with many alias lags in the posterior. We also require significant lags to be well-detected as 3σ different from zero, $|\tau| > 3\sigma_{\tau}$.

In summary, our criteria for statistically meaningful lags are as follows.

- 1. $f_{\rm peak} > 60\%$: A primary lag peak that includes at least 60% of the weighted lag posterior samples.
- 2. $|S/N(\tau)| > 3$: Minimum of 3σ difference from zero lag between the absolute value of the measured lag and its uncertainty. If the lag is positive, the noise is the lower bound uncertainty, and if the lag is negative, the noise is the upper bound uncertainty.

Figure 5 shows the lag measurement results for all 193 of our targets. The lag significance criteria are shown in each panel. There are 63 Mg II lags that meet the significant lag criteria,

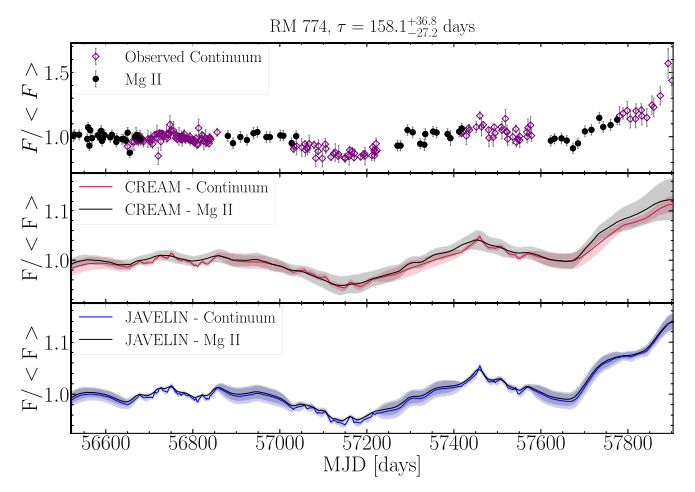


Figure 6. Overlapping continuum and Mg II lightcurves and best-fit CREAM and JAVELIN models for RM 774, with the Mg II lightcurve shifted by the measured lag. In this example, the lag is 158 days, such that the shifted Mg II observations fall within the seasonal gap of the continuum observations. However, the lag remains significant and well-constrained because the lightcurve has slow variations on multiyear timescales, such that the lag corresponds to periods in which both the continuum and shifted Mg II lightcurves are both varying in low- or high-flux states. Available as a figure set for the sample of 57 significant positive lags.

(The complete figure set (57 images) is available.)

with 57 positive lags (shown as red points in Figure 5). Table 1 reports the properties of these 57 quasars, drawn from Shen et al. (2019b).

As an additional check on the measured lags, Figure 6 presents the overlapping continuum and lag-shifted Mg II lightcurves and the CREAM and JAVELIN model fits. The overlapping lightcurves are especially instructive for lags of \sim 180 days in which the shifted Mg II observations fall in the seasonal gap of the photometric observations, casting doubt on the reliability of the lag detection. In general, these lags are associated with lightcurves that have smooth, low-frequency variations on multiyear timescales, like the example shown. In such cases, the lag posterior is well-constrained, with a strong primary peak corresponding to when both the continuum and shifted Mg II lightcurves are in low- or high-flux states. Significant lag detections of \sim 180 days can only be found for slow-varying lightcurves like the example shown in Figure 6. Lightcurves with variations on short timescales (i.e., highfrequency variability) require more overlap between shifted lightcurves for significant lag detection. Similar results have also been reported by Shen et al. (2019a) for C IV lightcurves.

4.3. Rate of False-positive Lags and "Gold Sample"

Large RM survey programs like SDSS-RM will inevitably include some number of false-positive lag detections. In particular, the limited cadence and seasonal gaps might allow for lag PDFs with well-defined peaks that meet our significant lag criteria but result from superpositions of nonreverberating lightcurves rather than genuine reverberation. We estimate the average false-positive rate of our lag detections by using the fact that our lag detection analysis does not include any preference for positive versus negative lags, with a lag search range and weighted prior that are both symmetric over $-1000 < \tau < 1000\,$ days. If the sample included only nonreverberating lightcurves and lag detections from spurious

overlapping lightcurves, the number of positive and negative lag detections would be equal. On the other hand, genuine broad-line reverberation should produce only positive lags.

Our sample includes a total of six negative and 57 positive lags that meet the significance criteria defined in Section 4.2. The negative lags are likely the result of spurious lightcurve correlations rather than broad-line reverberation, and the symmetric nature of our lag analysis means there is likely a similar number of spurious positive lags. Thus, we use the ratio of negative to positive lag detections as an estimate of the average false-positive rate: with six negative and 57 positive lags, the false-positive rate is 11%.

Figure 5 demonstrates that our sample includes significantly more positive than negative lags, even for lags below our significance criteria ($f_{\rm peak} > 60\%$ and $|{\rm S/N}(\tau)| > 3$). In the full sample, there are 149 positive and 44 negative lags, indicating an overall false-positive rate of 30%. The larger number of positive lags in the full sample indicates that an additional 40–50 of the positive lags are likely to be true positive lags. Many of these lower-significance positive lags are likely to become significant detections with additional SDSS-RM monitoring planned as part of the SDSS-V survey (Kollmeier et al. 2019).

The false-positive rate measured from the ratio of negative to positive lags is a robust indication of the overall sample reliability. However, not all lags in our sample are equally likely to correspond to physical reverberation or spurious correlations. To address this, we design an individual falsepositive rate test on all 193 set of lightcurves as a measure of each lag's likelihood of being true. We measure JAVELIN lag posteriors from each AGN continuum lightcurve matched to the Mg II lightcurve of a different AGN, repeating this process 100 times (and excluding duplications). Because the lightcurves from different AGN are uncorrelated, any lag detections meeting our significance criteria are false positives. The individual false-positive rates for the 57 positive significant lags are reported in Table 1 and shown in Figure 7. The average of the individual false-positive rates for the 57 positive significant lags is 11%, similar to the 11% false-positive rate for the sample measured from the ratio of significant negative to positive lags.

We use the individual false-positive rates to define a "gold sample" of the most reliable lag measurements with individual false-positive rates of $\leq 10\%$. The gold sample includes 24 significant, positive Mg II lags.

4.4. Lag Comparison: JAVELIN and CREAM

We test the reliability of our lag detections by comparing the results of JAVELIN and CREAM, as shown in Figure 8. In general, the two methods agree quite well: 60% of the significant JAVELIN lags have CREAM lags that agree within 1σ . In the full sample of significant positive and negative lags, there are a large number of outliers (21/63) that have JAVELIN and CREAM lags that differ by more than 3σ .

Visual inspection of the JAVELIN and CREAM model fits leads us to conclude that the JAVELIN results are more reliable. In many (8 out of 21) of the outlier cases where the lags disagree by more than 3σ , the CREAM lag fit fails to find a significant lag, with a lag posterior centered at $\tau \sim 0$ and/or with multiple peaks and $f_{\rm peak} < 60\%$. Recent work by Li et al. (2019) using simulated lightcurves similarly shows that JAVELIN typically outperforms other methods of lag

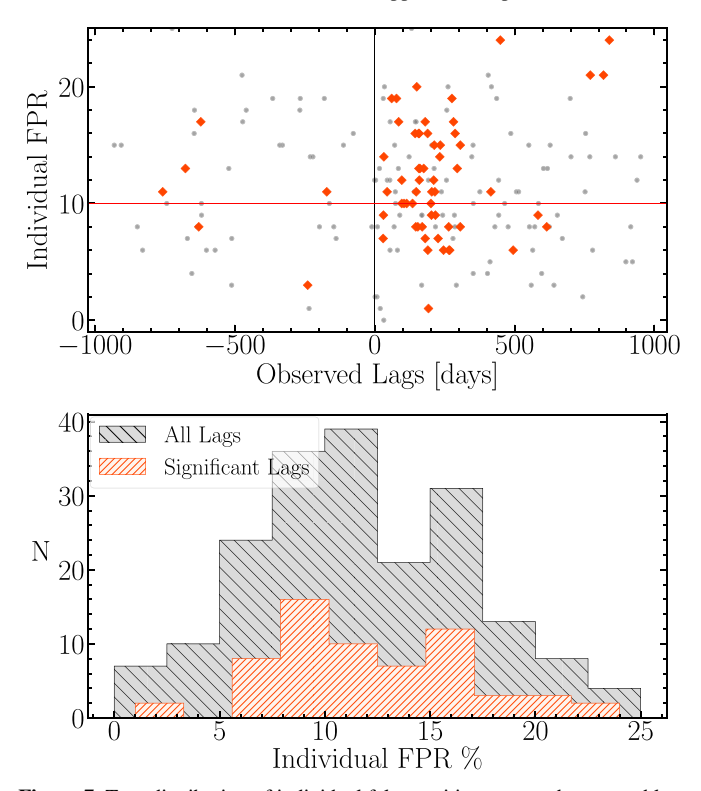


Figure 7. Top: distribution of individual false-positive rates and measured lags for the full sample (gray) and significant lags (red). False-positive rates are measured from matching each quasar continuum lightcurve with Mg II lightcurves of different quasars, repeated 100 times. Bottom: histogram of false-positive rates measured for full sample (gray) and the sample of significant lags (red). Significant lag sample has an average false-positive rate of 12% from this method, with a "gold sample" of 24 significant and positive lags with false-positive rates of $\leqslant 10\%$.

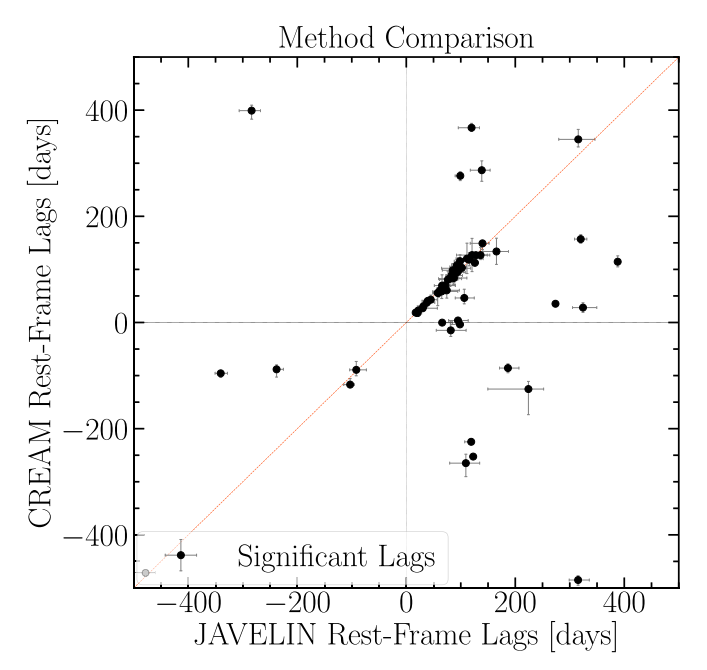


Figure 8. Comparison of lag measurements from JAVELIN and CREAM for the sample of 63 positive and negative lags that meet our significance criteria (defined in Section 4.2). Overall, CREAM and JAVELIN lag measurements are consistent within 1σ for 39 of the 63 significant lags (62%), although 33% of the lag solutions are outliers that differ by more than 3σ . In many of these outlier cases, the CREAM model fits find lags of $\sim\!\!0$ and/or with multiple peaks in the lag posterior that do not meet our significance criteria; only 13 lags are significant in both JAVELIN and CREAM and differ by more than 3σ .

identification, with more reliable lag uncertainties and lower false lag detections, for survey-quality RM observations.

We also compare our lag measurements with the six Mg II lags measured using only the 2014 SDSS-RM data by Shen et al. (2016b). We only recover the same lag for one of these six lags as a positive significant lag (RM 457). We find a lag consistent with Shen et al. (2016b) for two of the six (RM 101 and RM 229), but the lags do not meet our significance criteria because they have $f_{\text{peak}} < 0.6$. This is not surprising because Shen et al. (2016b) did not use a f_{peak} criterion for measuring lags. The remaining three objects (RM 589, RM 767, and RM 789) are more unusual: the 2014 lightcurves appear to be variable with Mg II reverberation, but the other three years have less variability and/or less apparent connection between the Mg II and continuum lightcurves, which result in the nondetection of a Mg II lag using the 4 yr data. These may be examples of anomalous BLR variability, sometimes referred to as "holiday states" (Dehghanian et al. 2019; Kriss et al. 2019), where the emission line stops reverberating with respect to the optical continuum.

5. Discussion

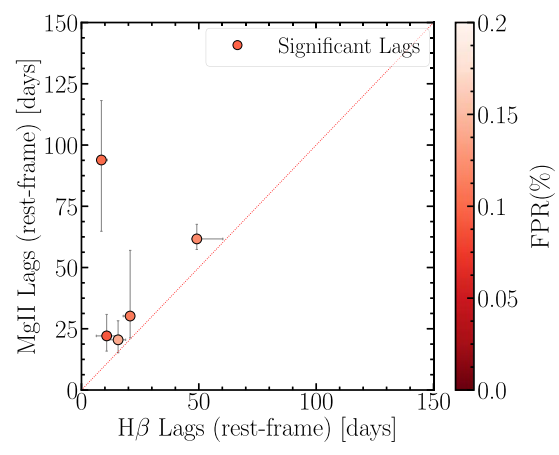
5.1. Stratification of the Broad-line Region

Reverberation mapping of multiple emission lines can reveal stratification of the broad-line region. Previous work has generally found that high-ionization lines like C IV and He II generally have shorter lags (i.e., lie closer to the ionizing continuum) while low-ionization lines like $H\beta$ and $H\alpha$ have longer lags (e.g., Clavel et al. 1991; Peterson & Wandel 1999; De Rosa et al. 2015). However, while its lower ionization suggests it is more likely to be emitted at larger radii, it is not clear how Mg II fits into the picture of BLR stratification. Unlike the recombination-dominated Balmer lines, the Mg II line includes significant collisional excitation, and it is expected to have lower responsivity and a broader response function (Goad et al. 1993; O'Brien et al. 1995; Korista & Goad 2000; Guo et al. 2020b). To date, there have been too few observations of Mg II lags to conclusively understand where the Mg II line sits relative to the rest of the BLR.

We compare our Mg II lags to published SDSS-RM H β (Grier et al. 2017) and C IV (Grier et al. 2019) lags in the same quasars in Figure 9. There are seven quasars with both H β and Mg II lags, and only one quasar with both C IV and Mg II lags. The small number of matches is due in part to the limited redshift range for observing both lines; having both C IV and Mg II is especially limiting because we restricted the Mg II sample to z < 1.7 to avoid variable sky line contamination. The H β -Mg II lag comparison is further limited by the 100 day search range of the Grier et al. (2017) H β lag sample, because it excludes longer H β lags that could be observed in quasars with longer Mg II lags.

To avoid this bias, we analyzed the 4 yr SDSS-RM lightcurves with JAVELIN to estimate H β lags for the three quasars with Mg II lags of >75 days. In one of these cases, we find the same lag as Grier et al. (2017), while the other two targets have $f_{\rm peak} < 60\%$ and the Grier et al. (2017) lags are coincident with secondary peaks in the lag posterior. The secondary lag peaks are likely due to additional variability features present in the multiyear data.

Furthermore, the measured lag may be different if the quasar luminosity changed significantly over multiple years of



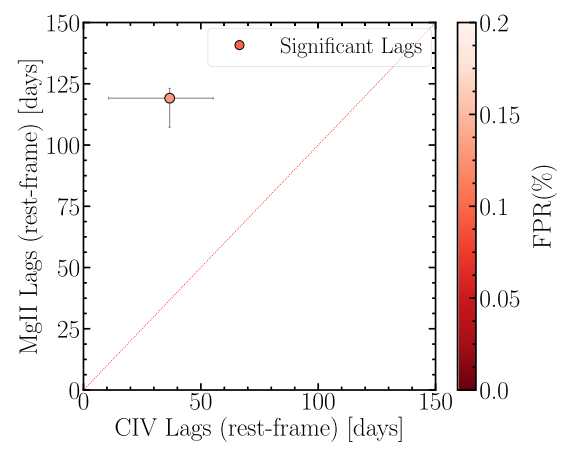


Figure 9. Comparison of five Mg II and H β lags (left) and single Mg II and C IV lags (right) for the quasars with significant lags from both this work and previous SDSS-RM studies (Grier et al. 2017, 2019). Limiting the comparison of Mg II and H β lags to the four objects with Mg II detectable within the 100 day search range of Grier et al. (2017), the ratio of Mg II to H β lags is 1.4 \pm 0.4. The single quasar in the right panel has a ratio of Mg II to C IV lag ratio of 3.2 \pm 0.6. In both cases, these comparisons are consistent with a stratified BLR, with the Mg II emission region at significantly larger radii than C IV and at radii similar to or marginally larger than H β .

observations. We remove the two sources with low- $f_{\rm peak}$ lags from the comparison and find a Mg II to H β lag ratio of 1.4 ± 0.4 (mean and uncertainty in the mean) for the remaining five objects. This ratio is consistent with the Mg II–emitting region being similar in size or marginally larger than the H β -emission region, and is also broadly consistent with previous Mg II lag measurements (Clavel et al. 1991; Czerny et al. 2019). A full analysis of the H β lags measured from the multiyear SDSS-RM data and their comparison to the Mg II lags measured here will appear in future work.

The single quasar with both Mg II and C IV lags, RM158, has a Mg II lag that is 3.2 ± 0.6 times longer than the C IV lag. The larger C IV lag is consistent with the BLR stratification model, where high-ionization lines such as C IV are at smaller radii compared to the low-ionization Mg II and H β lines.

5.2. The Mg II Radius-Luminosity Relation

Previous RM studies of H β and C IV have established empirical relations between the broad-line lags and the quasar continuum luminosity (Peterson et al. 2005; Kaspi et al. 2007; Bentz et al. 2013; Du et al. 2016b; Grier et al. 2017; Lira et al. 2018; Grier et al. 2019; Hoormann et al. 2019). These "radius–luminosity" relations have typically found a best-fit $R_{\rm BLR} \propto \lambda L_{\lambda}^{\alpha}$ consistent with a slope of $\alpha = 0.5$, as expected for a photoionization-driven BLR (Davidson 1972).

In contrast to H β and C IV, there has not yet been a sufficient number of Mg II lag measurements to construct a Mg II R-L relation. Compared to H β and C IV, attempts to measure RM Mg II lags have been affected by the smaller-amplitude variability of Mg II and its slower response to the continuum compared to the Balmer lines (i.e., Trevese et al. 2007; Woo 2008; Hryniewicz et al. 2014; Cackett et al. 2015). So far, there are only ~10 quasars with Mg II lag measurements (Clavel et al. 1991; Metzroth et al. 2006; Lira et al. 2018; Czerny et al. 2019), six of which come from the 2014 SDSS-RM observations (Shen et al. 2016b). Czerny et al. (2019) combine all the Mg II lag measurements from the literature and show that they are broadly consistent with the $H\beta$ radiusluminosity relation measured by Bentz et al. (2013), with a slope of $\alpha = 0.5$ and a Mg II broad-line size similar to that of $H\beta$.

We combine our new lag measurements with the existing Mg II lag measurements to fit an *R*–*L* relation

$$\log\left(\frac{R_{\rm BLR}}{\rm lt-days}\right) = \beta + \alpha \log\left(\frac{\lambda L_{3000}}{10^{44} \,\rm erg \, s^{-1}}\right). \tag{2}$$

To determine the best-fit R-L relation, we use the PyMc3 GLM robust linear regression method,²⁰ which takes a Bayesian approach to linear regression. We include an intrinsic scatter, σ , as a fitted parameter added in quadrature to the observed error. Our best-fit parameters to the gold sample and the significant lags sample are available in Table 2. This is similar to the intrinsic scatter model used in the FITEXY²¹ method of Kelly (2007).

Figure 10 shows the Mg II radius–luminosity relation for our new measurements and the three previous Mg II lags (compiled by Czerny et al. 2019). We use the 24 quasars from the gold sample along with the three existing Mg II lag measurements to find a best-fit Mg II radius-luminosity relation with a slope of $\alpha = 0.31^{+0.09}_{-0.10}$ and an intrinsic scatter of 0.36 dex (shown as the red line and gray envelope in Figure 10), the Mg II R-L best-fit slope is shallower but still marginally consistent (within 2σ) with the H β R-L best-fit line from Bentz et al. (2013), which lies within the uncertainties of our best-fit line in Figure 10. If we use the F test to quantify whether the slope α is necessary to model the data, we find that a luminosity-independent model $(\alpha \equiv 0)$ is rejected with a null probability of p = 0.002. This suggests that there exists an *R*–*L* relation for the Mg II emission line that is similar to $H\beta$, as expected for the basic photoionization expectation given the similar ionization potentials of H β (13.6 eV) and Mg II (15.0 eV). The radius– luminosity fit to all 57 significant positive lags has a shallower slope of $0.22^{+0.06}_{-0.05}$, but is likely affected by a larger number of false-positive lags.

The shallower slope of our Mg II R-L relation is similar to the shorter H β lags in SEAMBH and SDSS-RM quasars (Du et al. 2016b; Grier et al. 2017) compared to the Bentz et al. (2013) relation. As observed for the H β lags, the shallower best-fit slope may be caused by a range of quasar accretion

https://docs.pymc.io/notebooks/GLM-robust.html

²¹ https://github.com/jmeyers314/linmix

Table 1
Mg II Significant Lag Results

RMID	R.A.	Decl.	z	i-mag	SNR2	$\log \lambda L_{3000}$ $\log(\text{erg s}^{-1})$	$\tau_{\rm JAV}$	$f_{ m peak}$	FPR %	TCREAM	$\log M_{\rm BH}$	Gold Flag
	deg	deg					(days) Rest-frame		%	(days) Rest-frame	(M_{\odot})	
018	213.34694	53.1762	0.848	20.21	35	44.4	$125.9^{+6.8}_{-7.0}$	74	14	$112.5^{+7.5}_{-6.2}$	$9.14^{+0.16}_{-0.16}$	0
028	213.92953	52.84914	1.392	19.09	36	45.6	$65.7^{+24.8}_{-14.2}$	71	16	$69.5^{+20.2}_{-15.1}$	$8.51^{+0.23}_{-0.19}$	0
038	214.14908	52.94704	1.383	18.76	35	45.7	$120.7^{+27.9}_{-28.7}$	60	16	$127.0^{+31.5}_{-31.1}$	$8.73^{+0.19}_{-0.19}$	0
044	214.09516	53.30677	1.233	20.56	23	44.9	$65.8^{+18.8}_{-4.8}$	88	8	$-0.2^{+1.0}_{-1.3}$	$8.17^{+0.2}_{-0.16}$	1
102	213.47079	52.57895	0.861	19.54	31	45.0	$86.9^{+16.2}_{-13.3}$	90	13	$88.4^{+17.1}_{-16.8}$	$8.19^{+0.18}_{-0.17}$	0
114	213.89293	53.62056	1.226	17.73	43	46.1	$186.6^{+20.3}_{-15.4}$	67	11	$-85.9^{+7.9}_{-8.9}$	$9.12^{+0.17}_{-0.16}$	0
118	213.55325	52.53583	0.715	19.32	30	45.1	$102.2^{+27.0}_{-19.5}$	81	13	$-578.8^{+5.1}_{-1.7}$	$8.33^{+0.2}_{-0.18}$	0
123	214.65772	53.17155	0.891	20.44	26	44.7	$81.6^{+28.0}_{-26.6}$	95	8	$-14.8^{+17.6}_{-11.5}$	$8.7^{+0.22}_{-0.21}$	1
135	212.79563	52.80433	1.315	19.86	33	45.2	$93.0^{+9.6}_{-9.8}$	68	11	$107.9^{+10.7}_{-14.4}$	$8.22^{+0.17}_{-0.17}$	0
158	214.47802	53.54858	1.478	20.38	20	44.9	$119.1^{+4.0}_{-11.8}$	90	13	$-224.8_{-4.1}^{+6.0}$	$8.75^{+0.16}_{-0.17}$	0
159	213.69478	52.42325	1.587	19.45	34	45.5	$324.2^{+25.3}_{-19.4}$	76	24	$28.1^{+9.0}_{-8.9}$	$9.03^{+0.16}_{-0.16}$	0
160	212.67189	53.31361	0.36	19.68	189	43.8	$106.5^{+18.2}_{-16.6}$	94	16	$46.2^{+16.5}_{-11.2}$	$8.62^{+0.18}_{-0.17}$	0
170	214.52034	53.5496	1.163	20.17	30	45.2	$98.5^{+6.7}_{-17.7}$	91	15	$-3.6^{+4.5}_{-3.7}$	$9.2^{+0.16}_{-0.18}$	0
185	214.39977	52.5083	0.987	19.89	20	44.9	$387.9^{+3.3}_{-3.0}$	95	21	$114.5^{+10.9}_{-9.8}$	$9.36^{+0.16}_{-0.16}$	0
191	214.18991	53.74633	0.442	20.45	24	43.8	$93.9^{+24.3}_{-29.1}$	95	10	$102.1^{+15.0}_{-17.4}$	$8.31^{+0.2}_{-0.21}$	1
228	214.31267	52.38687	1.264	21.25	21	44.7	$37.9^{+14.4}_{-9.1}$	75	17	$37.5^{+5.7}_{-5.6}$	$8.34^{+0.23}_{-0.19}$	0
232	214.21357	52.34615	0.808	20.78	25	44.3	$273.8^{+5.1}_{-4.1}$	76	6	$35.3^{+5.9}_{-5.2}$	$9.0^{+0.17}_{-0.17}$	1
240	213.58696	52.27498	0.762	20.88	34	44.1	$17.2^{+3.5}_{-2.8}$	83	7	$18.6^{+1.5}_{-1.8}$	$8.11^{+0.18}_{-0.18}$	1
260	212.57517	52.57946	0.995	21.64	40	45.3	$94.9^{+18.7}_{-17.2}$	96	16	$3.8^{+4.4}_{-2.7}$	$8.12^{+0.18}_{-0.18}$	0
280	214.95499	53.53547	1.366	19.49	42	45.5	$99.1^{+3.3}_{-9.5}$	60	15	$276.3^{+7.5}_{-9.1}$	$8.51^{+0.16}_{-0.17}$	0
285	214.21215	52.25793	1.034	21.3	22	44.5	$138.5^{+15.2}_{-21.1}$	61	17	$286.8^{+17.5}_{-20.8}$	$8.54^{+0.17}_{-0.17}$	0
291	214.18017	52.24328	0.532	19.82	36	43.8	$39.7^{+4.2}_{-2.6}$	87	19	$40.8^{+3.3}_{-3.1}$	$8.67^{+0.17}_{-0.16}$	0
294	213.42134	52.20559	1.215	19.03	25	45.5	$71.8^{+17.8}_{-9.5}$	64	16	$70.4^{+8.1}_{-6.8}$	$8.37^{+0.19}_{-0.17}$	0
301	215.04269	52.6749	0.548	19.76	58	44.2	$136.3^{+17.0}_{-16.9}$	75	12	$127.0^{+14.1}_{-8.6}$	$9.09^{+0.17}_{-0.17}$	0
303	214.62585	52.37013	0.821	20.88	37	44.2	$57.7^{+10.5}_{-8.3}$	85	10	$55.7^{+9.3}_{-24.0}$	$8.72^{+0.18}_{-0.17}$	1
329	214.249	53.96852	0.721	18.11	47	45.4	$87.5^{+23.8}_{-14.0}$	69	20	$83.8^{+9.4}_{-9.1}$	$8.22^{+0.2}_{-0.18}$	0
338	214.98177	53.66865	0.418	20.08	20	43.8	$22.1^{+8.8}_{-6.2}$	92	9	$22.7^{+8.4}_{-5.5}$	$7.96^{+0.24}_{-0.2}$	1
419	213.00808	52.09101	1.272	20.35	21	45.0	$95.5^{+15.2}_{-15.5}$	77	9	$104.7^{+17.2}_{-21.1}$	$9.15^{+0.17}_{-0.18}$	1
422	211.9132	52.98075	1.074	19.72	31	44.7	$109.3^{+25.4}_{-29.6}$	72	7	$-264.9^{+16.9}_{-25.5}$	$8.99^{+0.19}_{-0.2}$	1
440	215.53806	53.09994	0.754	19.53	37	44.9	$114.6^{+7.4}_{-10.8}$	60	10	$118.7^{+6.7}_{-7.2}$	$9.03^{+0.16}_{-0.17}$	1
441	213.88294	51.98514	1.397	19.35	23	45.5	$127.7^{+5.7}_{-7.3}$	60	8	$126.8^{+3.2}_{-5.4}$	$8.19^{+0.16}_{-0.17}$	1
449	214.92398	53.93835	1.218	20.39	21	45.0	$119.8^{+14.7}_{-24.4}$	68	6	$366.8^{+8.3}_{-6.8}$	$8.9^{+0.17}_{-0.18}$	1
457	213.57136	51.95628	0.604	20.29	29	43.7	$20.5^{+7.7}_{-5.3}$	61	14	$17.6^{+7.0}_{-3.3}$	$7.73^{+0.23}_{-0.2}$	0
459	213.02897	54.14092	1.156	19.95	32	45.0	$122.8^{+5.1}_{-5.7}$	79	8	$-252.6^{+3.5}_{-3.2}$	$9.0^{+0.16}_{-0.16}$	1
469	215.27611	53.73527	1.004	18.31	38	45.6	$224.1^{+27.9}_{-74.3}$	63	24	$-125.4_{-48.3}^{+14.4}$	$9.08^{+0.17}_{-0.22}$	0
492	212.97555	52.0065	0.964	18.95	31	45.3	$92.0^{+16.3}_{-12.7}$	85	17	$94.5^{+11.9}_{-8.0}$	$8.63^{+0.18}_{-0.17}$	0
493	215.16448	52.32457	1.592	18.6	25	46.0	$315.6^{+30.7}_{-35.7}$	91	21	$344.9^{+18.8}_{-14.4}$	$9.56^{+0.17}_{-0.17}$	0
501	214.39663	51.98855	1.155	20.81	22	44.9	$44.9^{+11.7}_{-10.4}$	70	10	$42.9^{+8.6}_{-4.1}$	$8.49^{+0.2}_{-0.19}$	1
505	213.15791	51.95086	1.144	20.58	21	44.8	$94.7^{+10.8}_{-16.7}$	74	9	$95.6^{+11.1}_{-13.3}$	$9.2^{+0.17}_{-0.18}$	1
522	215.1741	52.28379	1.384	20.21	23	45.1	$115.8^{+11.3}_{-16.0}$	62	19	$119.1^{+12.3}_{-12.5}$	$8.26^{+0.17}_{-0.17}$	0
556	215.63556	52.66056	1.494	19.42	25	45.5	$98.7^{+13.9}_{-10.8}$	66	6	$115.5^{+11.9}_{-14.5}$	$8.69^{+0.17}_{-0.17}$	1
588	215.7673	52.77505	0.998	18.64	44	45.6	$74.3^{+23.0}_{-18.2}$	70	11	$60.6^{+12.7}_{-14.6}$	$8.21^{+0.21}_{-0.19}$	0
593	214.09805	51.82018	0.992	19.84	25	45.0	$80.1^{+21.4}_{-20.8}$	95	12	$82.6^{+16.7}_{-14.8}$	$8.03^{+0.2}_{-0.2}$	0
622	212.81328	51.86916	0.572	19.55	37	44.5	$61.7^{+6.0}_{-4.3}$	94	12	$60.0^{+3.9}_{-4.8}$	$7.7^{+0.17}_{-0.16}$	0
645	215.16582	52.06659	0.474	19.78	22	44.2	$30.2^{+26.8}_{-8.9}$	92	11	$26.8^{+15.0}_{-4.5}$	$8.2^{+0.42}_{-0.21}$	0
649	211.47859	52.89651	0.85	20.48	24	44.5	$165.5^{+22.2}_{-25.1}$	71	15	$133.7^{+25.1}_{-24.3}$	$8.8^{+0.17}_{-0.17}$	0
651	215.45543	52.24106	1.486	20.19	32	45.2	$76.5^{+18.0}_{-15.6}$	97	6	$80.9^{+16.0}_{-16.0}$	$8.67^{+0.19}_{-0.18}$	1
675	212.18248	54.13091	0.919	19.46	38	45.1	$139.8^{+12.0}_{-22.6}$	92	6	$149.1^{+3.6}_{-11.7}$	$9.26^{+0.17}_{-0.18}$	1
678	215.26356	52.07418	1.463	19.62	24	45.3	$82.9^{+11.9}_{-10.2}$	90	11	$88.4^{+11.7}_{-11.6}$	$8.52^{+0.17}_{-0.17}$	0
709	212.22948	51.9759	1.251	20.29	25	45.0	$85.4^{+17.7}_{-19.3}$	73	1	$98.4^{+12.7}_{-23.6}$	$8.57^{+0.19}_{-0.19}$	1
714	215.95717	52.65101	0.921	19.64	51	44.8	$320.1^{+11.3}_{-11.2}$	74	8	$157.1^{+8.3}_{-7.8}$	$9.45^{+0.16}_{-0.16}$	1
756	212.34759	51.85559	0.852	20.29	28	44.4	$315.3^{+20.5}_{-16.4}$	63	9	$-485.1^{+8.0}_{-9.7}$	$9.2^{+0.16}_{-0.16}$	1
761	216.05386	52.65096	0.771	20.43	48	44.8	$102.1^{+8.2}_{-7.4}$	64	7	$103.0^{+7.4}_{-6.6}$	$8.82^{+0.16}_{-0.16}$	1
771	214.01893	54.17766	1.492	18.64	42	45.7	$31.3^{+8.1}_{-4.6}$	85	19	$30.5^{+4.4}_{-4.8}$	$8.34^{+0.2}_{-0.17}$	0

Table 1 (Continued)

RMID	R.A. deg	Decl. deg	z	i-mag	SNR2	$\log \lambda L_{3000}$ $\log(\text{erg s}^{-1})$	τ _{JAV} (days) Rest-frame	f _{peak} %	FPR %	$ au_{ ext{CREAM}}$ (days) Rest-frame	$\log M_{ m BH} \ (M_{\odot})$	Gold Flag
774	212.62967	52.05463	1.686	19.34	29	45.7	58.9+13.7	95	13	55.5 ^{+6.2} _{-7.9}	$8.23^{+0.19}_{-0.18}$	0
792	214.503	53.3433	0.526	20.64	23	43.5	$111.4^{+29.5}_{-20.0}$	92	8	$120.3^{+29.2}_{-28.2}$	$8.98^{+0.2}_{-0.18}$	1
848	215.60674	53.57398	0.757	20.81	25	44.1	$65.1^{+29.4}_{-16.3}$	78	10	$58.5^{+15.8}_{-13.5}$	$8.24^{+0.25}_{-0.19}$	1

(This table is available in machine-readable form.)

Table 2 Mg II *R–L* Best Fit

Lag Sample	α	β	Intrinsic Scatter
Significant	$0.22^{+0.06}_{-0.05}$	$-7.95^{+5.52}_{-10.45}$	$0.30_{0.03}^{0.03}$
Gold	$0.31^{+0.10}_{-0.10}$	$-11.69^{+7.34}_{-16.07}$	$0.36^{+0.07}_{-0.05}$

rates and/or ionization conditions causing shorter Mg II lags (Du & Wang 2019; Fonseca Alvarez et al. 2020). It is likely that that shallower slope of the Mg II radius–luminosity relation is connected to its large intrinsic scatter, since large intrinsic scatter tends to lead to a shallower best-fit slope (e.g., Shen & Kelly 2010). On the other hand, Figure 10 shows that the upper limits in rest-frame lag detection (black crosses) are unlikely to affect the measured slope.

The best-fit Mg II R–L relation has a large excess scatter of 0.36 dex, significantly larger (by $> 2\sigma$) than the 0.25 dex excess scatter measured for the SDSS-RM H β lags (Fonseca Alvarez et al. 2020). This may be the result of the Mg II line having a significant collisional excitation component and/or a broader radial extent in the BLR (Goad et al. 1993; Korista & Goad 2000). Mg II is also a resonance line, so there could be radiative transfer effects that do not occur for H β line. A broader Mg II R–L relation than H β is also consistent with the predictions of the LOC photoionization models of Guo et al. (2020b), which shows that the Mg II emitting region is often located where the BLR is truncated and hence less affected by the continuum luminosity.

It would be interesting to investigate whether the lag offset from the Bentz et al. (2013) relation is connected to the Eddington ratio. Similar studies of the H β radius–luminosity relation demonstrate that quasars with higher Eddington ratio and/or higher ionization have shorter lags compared to the canonical R-L expectation (Du et al. 2016a; Fonseca Alvarez et al. 2020). However, we note that Eddington ratio selfcorrelates with both axes of the R-L relation and thus is not an independent quantity. A more suitable approach would be to adopt the relative iron strength as a proxy for Eddington ratio (e.g., Shen & Ho 2014). Optical Fe II strengths are unavailable in the SDSS spectra of most of our Mg II quasars, given their high redshifts, but Martínez-Aldama et al. (2020) instead found a relationship between relative UV Fe II strengths and R-L offset. We plan to further investigate how the Mg II R-L relation correlates with other quasar properties in future work.

Our new Mg II lag measurements occupy a convenient range of lags between the previous measurements of short lags in nearby low-luminosity Seyfert 1 AGN (Clavel et al. 1991; Metzroth et al. 2006) and the long lags measured for luminous quasars (Lira et al. 2018; Czerny et al. 2019). Future

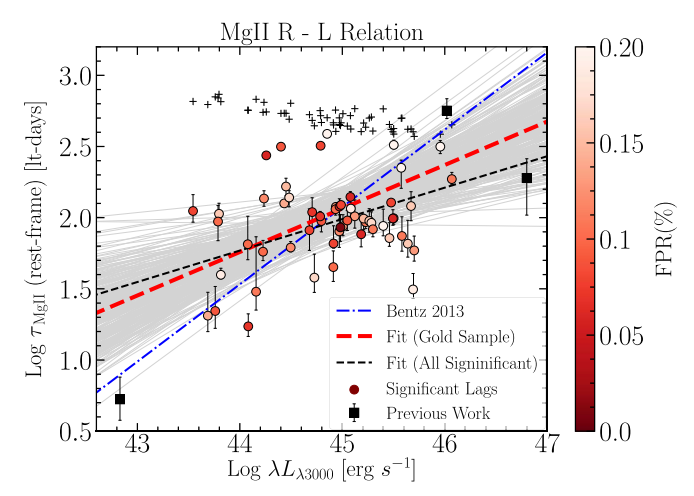


Figure 10. Mg II R-L relation for our new Mg II lags (circles, color-coded by individual false-positive rate) and previous measurements (black squares, compiled by Czerny et al. (2019)). Black cross symbols represent the upper limit in rest-frame lag computed from the observed-frame 1000 day search range and the target's redshift. Best-fit linear regression to the previous lags and our "gold sample" of lags (with individual false-positive rates of $\leq 10\%$) is shown by the dashed red line and has a slope of 0.31 ± 0.1 , with an excess intrinsic scatter of 0.36 dex. Gray shading indicates several samples of the MCMC fits. Best-fit line is shallower but marginally consistent (within 2σ) with the $\alpha = 0.533^{+0.035}_{-0.033}$ slope of the Bentz et al. (2013) best-fit H β R-L relation, although the Mg II R-L relation has significantly larger scatter. Fitting the entire sample, our 57 significant positive lags results in a shallower R-L relation with a slope of $0.22^{+0.06}_{-0.05}$, although this fit is likely affected by a larger number of false-positive lags than the gold sample.

monitoring of the SDSS-RM field with SDSS-V (Kollmeier et al. 2019) will cover a 10 yr monitoring baseline and add a larger number of longer lags from more luminous quasars.

5.3. Black Hole Masses at Cosmic High Noon

Over the last three decades, numerous campaigns have produced about 100 BH mass measurements from H β RM of broad-line AGN at z < 0.3 (e.g., the compilation of Bentz & Katz (2015)). Recent multiobject surveys like SDSS-RM have doubled this number, expanding the sample of H β RM masses to $z \sim 1$ (Shen et al. 2016b; Grier et al. 2017) and adding a large set of C IV RM masses at $z \sim 2$ (Grier et al. 2019). However, there still remains a large gap in RM mass measurements at 1 < z < 1.5, where Mg II is the only strong broad line available in an observed-frame optical spectrum. This redshift range is particularly important because the peak of SMBH total mass growth occurs within 1 < z < 2 (e.g., Aird et al. 2015).

With so few RM masses available, the bulk of BH masses over cosmic time have been estimated using scaling relations

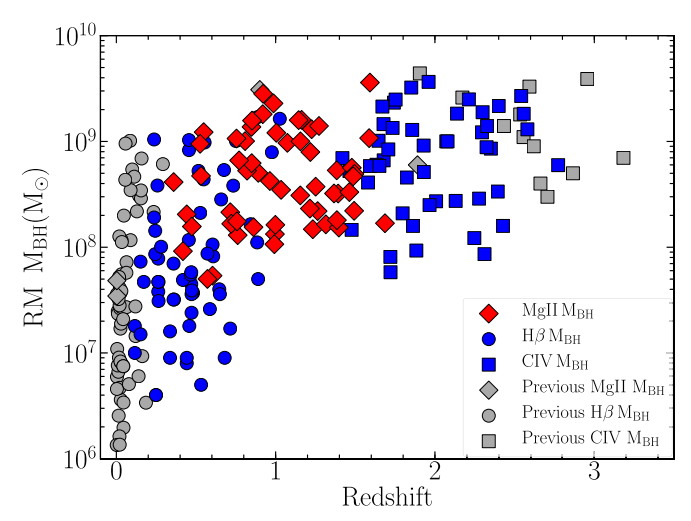


Figure 11. RM $M_{\rm BH}$ vs. redshift for AGNs with RM measurements. Different colored symbols represent the SDSS-RM $M_{\rm BH}$ measurements from H β (Grier et al. 2017), C IV (Grier et al. 2019), and Mg II (this work). Gray symbols illustrate the previous RM $M_{\rm BH}$ from the same emission lines (Kaspi et al. 2007; Bentz & Katz 2015; Du et al. 2016b; Lira et al. 2018; Czerny et al. 2019; Hoormann et al. 2019).

based on the observed H β R-L relation, substituting a singleepoch luminosity measurement for the expensive RM $R_{\rm BLR}$. Because the R–L relation is only well-measured for H β singleepoch masses, applying it to Mg II and C IV requires an additional scaling from H β line widths in quasars with both lines (McLure & Jarvis 2002; Vestergaard & Osmer 2009; Shen et al. 2011; Trakhtenbrot & Netzer 2012; Bahk et al. 2019). Even without this additional step, the uncertainty in H β single-epoch BH masses is at least 0.4 dex (Vestergaard & Peterson 2006; Shen 2013). The recently observed *R–L* offsets of H β lag measurements in more diverse AGN samples adds additional doubt that the H β *R*–*L* calibrated from previous RM samples describes the broader AGN population (Du et al. 2016b; Fonseca Alvarez et al. 2020). Finally, the previous lack of empirical data on the Mg II R-L relation raises the question of whether SE masses calibrated for H β are reliable for application to Mg II.

We compute RM-based BH masses for the 57 quasars with significant positive Mg II lags following Equation (1). Figure 11 shows the new Mg II mass measurements with previous RM $M_{\rm BH}$ from the SDSS-RM and other RM surveys. We use the Mg II $\sigma_{\rm line,rms}$ from PrepSpec for the line width, ΔV , and a virial factor f=4.47 from Woo et al. (2015). We follow the same approach as Grier et al. (2019) and compute the $M_{\rm BH}$ uncertainties by adding in quadrature the propagated lag and line width errors with an additional 0.16 dex uncertainty,

representing the typical uncertainty of RM-based masses from the uncertain f factor (Fausnaugh et al. 2016). The measured masses span $7.7 < \log(M_{\rm BH}/M_{\odot}) < 9.6$ and are included in Table 1.

Figure 12 compares the RM masses with single-epoch masses computed from the Shen et al. (2011) prescription (available in the SDSS-RM sample characterization catalog; see Shen et al. (2019b)). The RM and single-epoch masses are consistent within their large uncertainties, with an average ratio of 1.000 ± 0.003 and an excess scatter of 0.45. The agreement between RM and single-epoch masses is somewhat surprising, given the broad scatter in the Mg II radius–luminosity relation (Figure 10) and the multistep scaling required to derive the

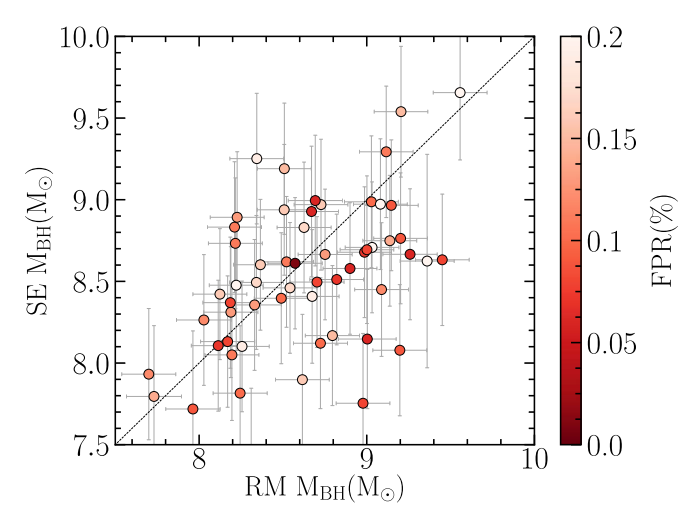


Figure 12. Single-epoch Mg II $M_{\rm BH}$ estimates from Shen et al. (2011) compared to the Mg II $M_{\rm BH}$ measurements from RM. Black dashed line shows a 1:1 ratio and measurements are color-coded by the individual false-positive rate.

Mg II single-epoch masses (e.g., Vestergaard & Osmer 2009). The agreement indicates that previous single-epoch masses measured from the Mg II line may be reasonable mass estimates within their large uncertainties.

6. Summary

We have used four years of SDSS-RM spectroscopic and photometric monitoring data to measure reverberation lags for the Mg II broad emission line. Starting from a sample of 193 quasars with well-detected Mg II variability (S/N > 20) in the redshift range 0.35 < z < 1.7, we use JAVELIN to measure significant positive lags in 57 quasars. Comparing the number of positive and negative significant lags suggests an average false-positive rate of 11% for the 57 lags. We additionally measure an individual false-positive rates for each quasar by performing JAVELIN analysis on shuffled continuum and Mg II lightcurves from different objects. We use these false-positive rates to define a "gold sample" of 24 lag measurements with individual false-positive rates \leq 10% as our most reliable lag measurements. Our major findings are as follows.

- 1. The new Mg II lags and previous SDSS-RM measurements of H β and C IV lags (Grier et al. 2017, 2019) in the same quasars are consistent with a stratified BLR, with Mg II lags that are a factor of a few larger than C IV lags and similar to or slightly larger than H β lags.
- 2. We find a radius–luminosity relation for Mg II with a best-fit slope that is shallower but marginally consistent (within 2σ) with $\alpha=0.5$, and with 0.4 dex of scatter that is significantly larger than the scatter observed in the H β radius–luminosity relation. This implies a broader range of Mg II radii than observed for H β , consistent with BLR excitation models (Goad et al. 1993; O'Brien et al. 1995; Korista & Goad 2000; Guo et al. 2020b).
- 3. We compute RM-based BH masses for the 57 significant positive lags using the measured Mg II FWHM and find that the single-epoch masses produced by the prescription of Shen et al. (2011) are consistent with the RM masses.

The lack of Mg II RM measurements at the peak of SMBH growth is among the pressing problems in RM measurements. This work provides the first large set of Mg II mass

measurements that covers the gap between $H\beta$ and C IV in optical RM studies. Future work will further study BLR stratification using the multiyear SDSS-RM data to measure $H\beta$ lags on a longer monitoring baseline that is comparable to the Mg II lag measurement limits of this work. We will also further investigate the Mg II radius–luminosity relation, using simulations (Li et al. 2019; Fonseca Alvarez et al. 2020) to understand its shallower slope and large scatter.

Y. H., J. R. T., and G. F. A. acknowledge support from NASA grants *HST*-GO-15650 and 18-2ADAP18-0177 and NSF grant CAREER-1945546. Y. S., D. A. S., and J. L. acknowledge support from an Alfred P. Sloan Research Fellowship (Y. S.) and NSF grant AST-1715579. K. H. and J. V. H. S. acknowledge support from STFC grant ST/R000824/1. P. H. acknowledges support from the Natural Sciences and Engineering Research Council of Canada (NSERC), funding reference number 2017-05983, and from the National Research Council Canada during his sabbatical at NRC Herzberg Astronomy & Astrophysics. L. C. H. was supported by the National Key R&D Program of China (2016YFA0400702) and the National Science Foundation of China (11473002, 11721303). C. S. K. acknowledges support from NSF grants AST-1908952 and AST-1814440.

Funding for SDSS-III was provided by the Alfred P. Sloan Foundation, the Participating Institutions, the National Science Foundation, and the U.S. Department of Energy Office of Science. The SDSS-III website is http://www.sdss3.org/. SDSS-III was managed by the Astrophysical Research Consortium for the Participating Institutions of the SDSS-III Collaboration including the University of Arizona, the Brazilian Participation Group, Brookhaven National Laboratory, Carnegie Mellon University, University of Florida, the French Participation Group, the German Participation Group, Harvard University, the Instituto de Astrofisica de Canarias, the Michigan State/Notre Dame/JINA Participation Group, The Johns Hopkins University, Lawrence Berkeley National Laboratory, Max Planck Institute for Astrophysics, Max Planck Institute for Extraterrestrial Physics, New Mexico State University, New York University, Ohio State University, Pennsylvania State University, University of Portsmouth, Princeton University, the Spanish Participation Group, University of Tokyo, University of Utah, Vanderbilt University, University of Virginia, University of Washington, and Yale University.

Funding for SDSS-IV has been provided by the Alfred P. Sloan Foundation, the U.S. Department of Energy Office of Science, and the Participating Institutions. SDSS acknowledges support and resources from the Center for High-Performance Computing at the University of Utah. The SDSS website is www.sdss.org. SDSS is managed by the Astrophysical Research Consortium for the Participating Institutions of the SDSS Collaboration including the Brazilian Participation Group, the Carnegie Institution for Science, Carnegie Mellon University, the Chilean Participation Group, the French Participation Group, Harvard-Smithsonian Center for Astrophysics, Instituto de Astrofísica de Canarias, The Johns Hopkins University, Kavli Institute for the Physics and Mathematics of the Universe (IPMU)/University of Tokyo, the Korean Participation Group, Lawrence Berkeley National Laboratory, Leibniz Institut für Astrophysik Potsdam (AIP), Max-Planck-Institut für Astronomie (MPIA Heidelberg),

Max-Planck-Institut für Astrophysik (MPA Garching), Max-Planck-Institut für Extraterrestrische Physik (MPE), National Astronomical Observatories of China, New Mexico State University, New York University, University of Notre Dame, Observatório Nacional/MCTI, The Ohio State University, Pennsylvania State University, Shanghai Astronomical Observatory, United Kingdom Participation Group, Universidad Nacional Autónoma de México, University of Arizona, University of Colorado Boulder, University of Oxford, University of Portsmouth, University of Utah, University of Virginia, University of Washington, University of Wisconsin, Vanderbilt University, and Yale University.

We thank the Bok and CFHT Canadian, Chinese, and French TACs for their support. This research uses Bok data obtained through the Telescope Access Program (TAP), which is funded by the National Astronomical Observatories, Chinese Academy of Sciences, and the Special Fund for Astronomy from the Ministry of Finance in China. This work is based on observations obtained with MegaPrime/MegaCam, a joint project of CFHT and CEA/DAPNIA, at the Canada-France-Hawaii Telescope (CFHT), which is operated by the National Research Council (NRC) of Canada, the Institut National des Sciences de l'Univers of the Centre National de la Recherche Scientifique of France, and the University of Hawaii. The authors wish to recognize and acknowledge the very significant cultural role and reverence that the summit of Maunakea has always had within the indigenous Hawaiian community. The astronomical community is most fortunate to have the opportunity to conduct observations from this mountain.

Software: PrepSpec, ISIS (Alard & Lupton 1998; Alard 2000), CREAM (Starkey et al. 2016), BOSS reduction pipeline (Dawson et al. 2016; Blanton et al. 2017), Javelin (Zu et al. 2011), PyceCREAM (https://github.com/dstarkey23/pycecream), linmix (https://github.com/jmeyers314/linmix), PyMc3 (https://docs.pymc.io/notebooks/GLM-robust.html).

ORCID iDs

Y. Homayouni https://orcid.org/0000-0002-0957-7151 Jonathan R. Trump https://orcid.org/0000-0002-1410-0470 C. J. Grier https://orcid.org/0000-0001-9920-6057 Keith Horne https://orcid.org/0000-0003-1728-0304 Yue Shen https://orcid.org/0000-0003-1659-7035 W. N. Brandt https://orcid.org/0000-0002-0167-2453 Kyle S. Dawson https://orcid.org/0000-0002-0553-3805 Paul J. Green https://orcid.org/0000-0002-8179-9445 P. B. Hall https://orcid.org/0000-0002-1763-5825 Juan V. Hernández Santisteban https://orcid.org/0000-0002-6733-5556 Luis C. Ho https://orcid.org/0000-0001-6947-5846 Karen Kinemuchi https://orcid.org/0000-0001-7908-7724 C. S. Kochanek https://orcid.org/0000-0001-6017-2961 Jennifer I-Hsiu Li https://orcid.org/0000-0002-0311-2812 B. M. Peterson https://orcid.org/0000-0001-6481-5397 D. P. Schneider https://orcid.org/0000-0001-7240-7449 Dmitry Bizyaev https://orcid.org/0000-0002-3601-133X Kaike Pan https://orcid.org/0000-0002-2835-2556 Audrey Simmons https://orcid.org/0000-0002-2364-7240

References

Aird, J., Coil, A. L., Georgakakis, A., et al. 2015, MNRAS, 451, 1892
Alard, C. 2000, A&AS, 144, 363
Alard, C., & Lupton, R. H. 1998, ApJ, 503, 325

```
Aune, S., Boulade, O., Charlot, X., et al. 2003, Proc. SPIE, 4841, 513
Bahk, H., Woo, J.-H., & Park, D. 2019, ApJ, 875, 50
Barth, A. J., Bennert, V. N., Canalizo, G., et al. 2015, ApJS, 217, 26
Bentz, M. C., Denney, K. D., Grier, C. J., et al. 2013, ApJ, 767, 149
Bentz, M. C., & Katz, S. 2015, PASP, 127, 67
Bentz, M. C., Walsh, J. L., Barth, A. J., et al. 2009, ApJ, 705, 199
Bentz, M. C., Walsh, J. L., Barth, A. J., et al. 2010, ApJ, 716, 993
Blandford, R. D., & McKee, C. F. 1982, ApJ, 255, 419
Blanton, M. R., Bershady, M. A., Abolfathi, B., et al. 2017, AJ, 154, 28
Brandt, W. N., & Alexander, D. M. 2015, A&ARv, 23, 1
Cackett, E. M., Gültekin, K., Bentz, M. C., et al. 2015, ApJ, 810, 86
Cackett, E. M., & Horne, K. 2006, MNRAS, 365, 1180
Cackett, E. M., Horne, K., & Winkler, H. 2007, MNRAS, 380, 669
Clavel, J., Reichert, G. A., Alloin, D., et al. 1991, ApJ, 366, 64
Czerny, B., Olejak, A., Ralowski, M., et al. 2019, ApJ, 880, 46
Davidson, K. 1972, ApJ, 171, 213
Dawson, K. S., Kneib, J.-P., Percival, W. J., et al. 2016, AJ, 151, 44
Dawson, K. S., Schlegel, D. J., Ahn, C. P., et al. 2013, AJ, 145, 10
De Rosa, G., Peterson, B. M., Ely, J., et al. 2015, ApJ, 806, 128
Dehghanian, M., Ferland, G. J., Kriss, G. A., et al. 2019, ApJ, 877, 119
Denney, K. D., Horne, K., Brandt, W. N., et al. 2016a, ApJ, 833, 33
Denney, K. D., Horne, K., Shen, Y., et al. 2016b, ApJS, 224, 14
Denney, K. D., Peterson, B. M., Pogge, R. W., et al. 2010, ApJ, 721, 715
Dexter, J., Xin, S., Shen, Y., et al. 2019, ApJ, 885, 44
Doi, M., Tanaka, M., Fukugita, M., et al. 2010, AJ, 139, 1628
Du, P., Hu, C., Lu, K.-X., et al. 2015, ApJ, 806, 22
Du, P., Lu, K.-X., Hu, C., et al. 2016a, ApJ, 820, 27
Du, P., Lu, K.-X., Zhang, Z.-X., et al. 2016b, ApJ, 825, 126
Du, P., & Wang, J.-M. 2019, ApJ, 886, 42
Event Horizon Telescope Collaborationz, Akiyama, K., Alberdi, A., et al.
   2019, ApJL, 875, L6
Fausnaugh, M. M., Denney, K. D., Barth, A. J., et al. 2016, ApJ, 821, 56
Fonseca Alvarez, G., Trump, J. R., Homayouni, Y., et al. 2020, ApJ, 899, 73
Fukugita, M., Ichikawa, T., Gunn, J. E., et al. 1996, AJ, 111, 1748
Gaskell, C. M., & Peterson, B. M. 1987, ApJS, 65, 1
Gaskell, C. M., & Sparke, L. S. 1986, ApJ, 305, 175
Goad, M. R., O'Brien, P. T., & Gondhalekar, P. M. 1993, MNRAS, 263, 149
Grier, C. J., Brandt, W. N., Hall, P. B., et al. 2016, ApJ, 824, 130
Grier, C. J., Peterson, B. M., Horne, K., et al. 2013, ApJ, 764, 47
Grier, C. J., Peterson, B. M., Pogge, R. W., et al. 2012, ApJ, 755, 60
Grier, C. J., Shen, Y., Horne, K., et al. 2019, ApJ, 887, 38
Grier, C. J., Trump, J. R., Shen, Y., et al. 2017, ApJ, 851, 21
Gültekin, K., Richstone, D. O., Gebhardt, K., et al. 2009, ApJ, 698, 198
Gunn, J. E., Siegmund, W. A., Mannery, E. J., et al. 2006, AJ, 131, 2332
Guo, H., Shen, Y., He, Z., et al. 2020a, ApJ, 888, 58
Guo, H., Shen, Y., He, Z., et al. 2020b, ApJ, 888, 58
Hemler, Z. S., Grier, C. J., Brandt, W. N., et al. 2019, ApJ, 872, 21
Homayouni, Y., Trump, J. R., Grier, C. J., et al. 2019, ApJ, 880, 126
Hoormann, J. K., Martini, P., Davis, T. M., et al. 2019, MNRAS, 487, 3650
Hryniewicz, K., Czerny, B., Pych, W., et al. 2014, A&A, 562, A34
Hu, C., Du, P., Lu, K.-X., et al. 2015, ApJ, 804, 138
Kaspi, S., Brandt, W. N., Maoz, D., et al. 2007, ApJ, 659, 997
Kaspi, S., Smith, P. S., Netzer, H., et al. 2000, ApJ, 533, 631
Kelly, B. C. 2007, ApJ, 665, 1489
Kelly, B. C., Bechtold, J., & Siemiginowska, A. 2009, ApJ, 698, 895
```

```
Kinemuchi, K., Hall, P. B., McGreer, I., et al. 2020, ApJS, 250, 10
Kollmeier, J., Anderson, S. F., Blanc, G. A., et al. 2019, BAAS, 51, 274
Korista, K. T., & Goad, M. R. 2000, ApJ, 536, 284
Kormendy, J., & Ho, L. C. 2013, ARA&A, 51, 511
Kozłowski, S. 2016, ApJ, 826, 118
Kriss, G. A., De Rosa, G., Ely, J., et al. 2019, ApJ, 881, 153
Li, J., Shen, Y., Brandt, W. N., et al. 2019, ApJ, 884, 119
Lira, P., Kaspi, S., Netzer, H., et al. 2018, ApJ, 865, 56
MacLeod, C. L., Ivezić, Ž., Kochanek, C. S., et al. 2010, ApJ, 721, 1014
MacLeod, C. L., Ivezić, Ž., Sesar, B., et al. 2012, ApJ, 753, 106
Magorrian, J., Tremaine, S., Richstone, D., et al. 1998, AJ, 115, 2285
Martínez-Aldama, M. L., Zajaĉek, M., Czerny, B., & Panda, S. 2020,
  arXiv:2007.09955
Matsuoka, Y., Strauss, M. A., Shen, Y., et al. 2015, ApJ, 811, 91
McLure, R. J., & Jarvis, M. J. 2002, MNRAS, 337, 109
Metzroth, K. G., Onken, C. A., & Peterson, B. M. 2006, ApJ, 647, 901
O'Brien, P. T., Goad, M. R., & Gondhalekar, P. M. 1995, MNRAS, 275, 1125
Pancoast, A., Barth, A. J., Horne, K., et al. 2018, ApJ, 856, 108
Pei, L., Fausnaugh, M. M., Barth, A. J., et al. 2017, ApJ, 837, 131
Peterson, B. M. 1993, PASP, 105, 247
Peterson, B. M. 2004, in IAU Symp. 222, The Interplay Among Black Holes,
  Stars and ISM in Galactic Nuclei, ed. T. Storchi-Bergmann, L. C. Ho, &
  H. R. Schmitt (Cambridge: Cambridge Univ. Press), 15
Peterson, B. M., Balonek, T. J., Barker, E. S., et al. 1991, ApJ, 368, 119
Peterson, B. M., Bentz, M. C., Desroches, L.-B., et al. 2005, ApJ, 632,
  799
Peterson, B. M., & Wandel, A. 1999, ApJL, 521, L95
Reichert, G. A., Rodriguez-Pascual, P. M., Alloin, D., et al. 1994, ApJ,
  425, 582
Shen, Y. 2013, BASI, 41, 61
Shen, Y., Brandt, W. N., Dawson, K. S., et al. 2015a, ApJS, 216, 4
Shen, Y., Brandt, W. N., Richards, G. T., et al. 2016a, ApJ, 831, 7
Shen, Y., Greene, J. E., Ho, L. C., et al. 2015b, ApJ, 805, 96
Shen, Y., Grier, C. J., Horne, K., et al. 2019a, ApJL, 883, L14
Shen, Y., Hall, P. B., Horne, K., et al. 2019b, ApJS, 241, 34
Shen, Y., & Ho, L. C. 2014, Natur, 513, 210
Shen, Y., Horne, K., Grier, C. J., et al. 2016b, ApJ, 818, 30
Shen, Y., & Kelly, B. C. 2010, ApJ, 713, 41
Shen, Y., & Kelly, B. C. 2012, ApJ, 746, 169
Shen, Y., Richards, G. T., Strauss, M. A., et al. 2011, ApJS, 194, 45
Smee, S. A., Gunn, J. E., Uomoto, A., et al. 2013, AJ, 146, 32
Starkey, D. A., Horne, K., & Villforth, C. 2016, MNRAS, 456, 1960
Sun, M., Trump, J. R., Shen, Y., et al. 2015, ApJ, 811, 42
Trakhtenbrot, B., & Netzer, H. 2012, MNRAS, 427, 3081
Trevese, D., Paris, D., Stirpe, G. M., Vagnetti, F., & Zitelli, V. 2007, A&A,
  470, 491
Vestergaard, M., & Osmer, P. S. 2009, ApJ, 699, 800
Vestergaard, M., & Peterson, B. M. 2006, ApJ, 641, 689
Wang, S., Shen, Y., Jiang, L., et al. 2019, ApJ, 882, 4
Williams, G. G., Olszewski, E., Lesser, M. P., & Burge, J. H. 2004, Proc. SPIE,
  5492, 787
Woo, J.-H. 2008, AJ, 135, 1849
Woo, J.-H., Yoon, Y., Park, S., Park, D., & Kim, S. C. 2015, ApJ, 801, 38
Yu, Z., Kochanek, C. S., Peterson, B. M., et al. 2020, MNRAS, 491, 6045
Zu, Y., Kochanek, C. S., & Peterson, B. M. 2011, ApJ, 735, 80
```